Acta Cryst. (1997). A**53**, 341-351

The Defect Character of Carbon Nanotubes and Nanoparticles

G. P. DIMITRAKOPULOS,[a] V. P. DRAVID,[b] TH. KARAKOSTAS[a]* AND R. C. POND[c]

[a]*Aristotle University of Thessaloniki, Department of Physics, Solid State Physics Section, GR 540 06 Thessaloniki, Greece,* [b]*Materials Research Center, Northwestern University, Evanston, IL 60208, USA, and* [c]*University of Liverpool, Department of Materials Science and Engineering, Liverpool L69 3BX, England. E-mail: karakost@ccf.auth.gr*

(*Received 7 September 1996; accepted 7 January 1997*)

Abstract

Circuit mapping is employed to study the defect content of buckytubes and carbon nanoparticles. The topological analysis enables the connection with the well established defect theory of crystalline materials. The complementarity between defect models of two- and three-dimensional structures is considered as well as the significance of dislocation descriptions of these materials. In accordance with recent experimental observations, the possibility of three-dimensional hexagonal graphitic stacking of atoms in these structures is examined through the introduction of appropriate defects that are admissible in graphite. Defects in graphene sheets introduce cap closure of isolated tubules and changes in tubule orientation, radius and helicity. In multilayered tubes, appropriate defects can accommodate curvature among adjacent sheets so that the ...*ABAB*... stacking is preserved. However, the graphite stacking is generally destroyed in multilayered caps owing to the lack of appropriate graphite defects for their accommodation.

1. Introduction

The discovery of carbon buckminsterfullerenes (Kroto, Heath, O'Brien, Curl & Smalley, 1985) and nanotubes (Iijima, 1991) has created a new area of interest in materials science, especially for applications in fields such as electronics and composites (Dresselahaus, 1992; Ebbesen, 1994; Ruoff, 1994). It has been appreciated that the properties of carbon cages in the fullerene family are structure-dependent. For example, it has been claimed that carbon nanotubes (or buckytubes) can exhibit various conductivities depending on their radius and helicity (Hamada, Sawada & Oshiyama, 1992; Saito, Fujita, Dresselahaus & Dresselahaus, 1992; Olk & Heremans, 1994). These conclusions have been questioned by others, in particular with respect to whether they are valid for nanotubes composed of more than a few graphene layers (Blase, Benedict, Shirley & Louie, 1994; Bursill, Stadelmann, Peng & Prawer, 1994; Bursill, Peng & Fan, 1995). Other properties have also been shown to be structure sensitive (Tsang, Harris & Green, 1993; Lu, 1995).

Carbon cages have been observed to acquire the morphologies of (single- or multilayered) spheres, tubes and nanoparticles or 'onions' (Ugarte, 1992; Clinard, Rouzaud, Delpeux, Beguin & Conard, 1994; Xie *et al.*, 1995). Several authors have interpreted their structures in terms of defects, particularly disclinations associated with pentagons or heptagons in two-dimensional arrays of hexagons representing sp^2 bonding in graphene sheets (Iijima, Ichihashi & Ando, 1992; Clinard, Rouzaud, Delpeux, Beguin & Conard, 1994). This has been shown to be useful, especially for discussion of the curvature of graphene sheets into convoluted and closed forms. The concept of dislocations has also been used to explain the accommodation of strains in adjacent sheets when multilayering occurs and to explain the often observed polygonization of nanoparticles and buckytubes with large radii (Zhang *et al.*, 1993). Other authors have explained this phenomenon by presenting geometrical arguments and experimental evidence for perturbations of graphene sheets involving chain configurations of sp^3 bonding (Harris, Green & Tsang, 1993).

In the work outlined above, a graphene sheet is treated essentially as a two-dimensional entity that interacts very weakly with adjacent sheets if present. On the other hand, a large body of recent evidence suggests that interaction between layers can be of greater significance; multilayered nanotubes and nanoparticles may exhibit a graphitic arrangement of adjacent layers, at least locally. Such evidence includes the preservation of the ...*ABAB*... stacking and spacing, as well as polygonization of tubes and particles (Liu & Cowley, 1994; Bursill, Peng & Fan, 1995; Reznik, Olk, Neumann & Copley, 1995). In such circumstances, defects characteristic of three-dimensional structures become feasible and initial experimental observations have been reported (Dravid *et al.*, 1993; Harris, Green & Tsang, 1993; Bursill, Peng & Fan, 1995; Xie *et al.*, 1995).

The object of the present work is to investigate the complementarity between defect models of two- and three-dimensional structures and to consider the significance of dislocation descriptions of carbon nanotubes and nanoparticles. For our purpose, we perform a topological analysis using the method of circuit mapping; this enables the connection with the well established theory

of line defects in crystalline materials. In our account, we consider the tubule arrangement models observed and proposed so far, *i.e.* the model of coaxial seamless tubules (Iijima, 1991; Iijima, Ichihashi & Ando, 1992; Zhang *et al.*, 1993), the scroll (Harris, Green & Tsang, 1993), and the papier-mâché model (Bursill, Peng & Fan, 1995; Zhou *et al.*, 1994). In all cases, consideration of helicity is important as helicity has been shown to have a role in defining electric properties. In §2, an account of defects in two-dimensional structures is given. In §3, we examine defects in three-dimensional multilayered structures for a graphitic alignment of adjacent layers. The conclusions are discussed in §4.

2. Defects in two-dimensional structures

2.1. *Disclinations and dislocations in graphene sheets*

Defects can be characterized topologically by the method of circuit mapping, introduced initially by Frank (1951) and developed more recently by others, *e.g.* Pond & Hirth (1994). The procedure generally is to construct a closed circuit of discrete motions in the distorted configuration and subsequently to map this circuit into a reference space; the nature of any closure failure in the mapped circuit characterizes the defect encircled in the original circuit. In the present context, the reference spaces for two- and three-dimensional structures are the space groups for an infinite graphene sheet, *p6mm*, and for graphite, $P6_3/mmc$, respectively. These spaces are depicted schematically in Fig. 1. In this subsection, we illustrate the characterization of disclinations in graphene using circuit mapping and we demonstrate their equivalent descriptions in terms of dislocation arrays. We also show how a disclination's strain field can be annihilated by the introduction of appropriate defects. This information is then used to study the defect character of isolated seamless tubules.

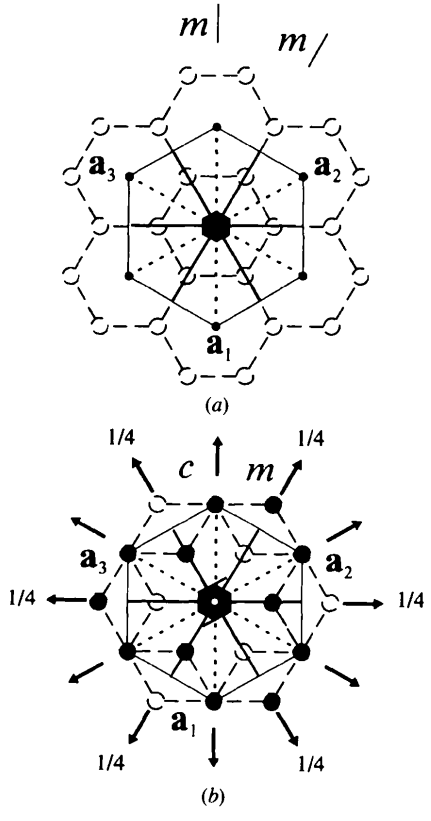

Fig. 1. (*a*) The two-dimensional structure of graphene (symmetry *p6mm*). Symmetry elements are shown superimposed on the underlying structure (dashed) and, in particular, the projections of $\{1\bar{1}00\}$ mirrors (dotted) and $\{2\bar{1}\bar{1}0\}$ mirrors. Small black circles denote lattice points. The lattice translations $\mathbf{a}_1 = 1/3[2\bar{1}\bar{1}0]$, $\mathbf{a}_2 = 1/3[\bar{1}2\bar{1}0]$ and $\mathbf{a}_3 = 1/3[\bar{1}\bar{1}20]$ are also shown. (*b*) [0001] projection of the graphite structure (symmetry $P6_3/mmc$). Black and white circles denote atoms at height $\pm 1/4$[0001]. Dotted lines denote $\{1\bar{1}00\}$ mirror-glide planes. Arrows denote twofold symmetry axes.

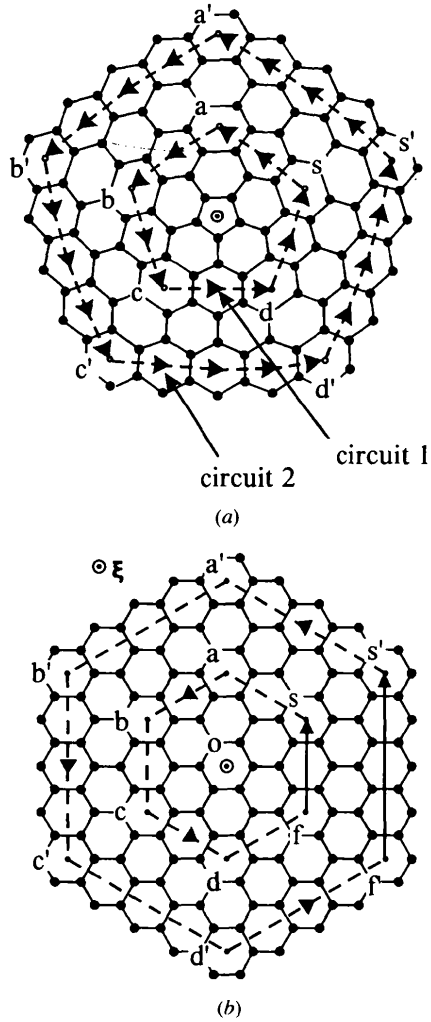

Fig. 2. (*a*) Closed circuits drawn around a positive wedge disclination in a graphene sheet. (*b*) The same circuits mapped in the reference space. Closure failures **fs** and **f's'** arise.

Consider a positive wedge disclination in graphene and imagine an observer to undergo the journey *s–a–b–c–d–s* (circuit 1) in direct space, as indicated in Fig. 2(*a*). All locations visited in this excursion are crystallographically equivalent to him, and hence the circuit appears to comprise a sequence of symmetry operations. This sequence maps to circuit *s–a–b–c–d–f* in the reference space as shown in Fig. 2(*b*); thus, there is a closure failure equal to **fs**. A second circuit s'–a'–b'–c'–d'–s' (circuit 2) and its mapped counterpart are shown in Figs. 2(*a*) and (*b*), respectively; the new closure failure is $\mathbf{f's'}$. The closure failure is obtained mathematically as follows: Let the observer begin the journey at point *s* located at $2/3[\bar{1}2\bar{1}0]$ (using Miller–Bravais indexing), with respect to the origin (Fig. 2). In addition, let the observer's coordinate frame have the same orientation as the reference frame at the outset; thus, his initial orientation and location are defined by $(\mathbf{I}, \mathbf{s})$, where $\mathbf{I}$ represents the identity matrix. Symmetry operations in the sequence are designated $\mathcal{W} = (\mathbf{W}, \mathbf{w})$, using the notation of *International Tables for Crystallography* (Hahn, 1983). A symmetry operation acting on the observer when at a location $\mathbf{r}$ is written $\mathcal{W}^* = (\mathbf{I}, \mathbf{r})\mathcal{W}(\mathbf{I}, \mathbf{r})^{-1}$. Thus, a sequence of operations can be written $\mathcal{C} = \mathcal{W}_n^*, \ldots, \mathcal{W}_2^*\mathcal{W}_1^*$, where the overall sequence operator $\mathcal{C} = (\mathbf{C}, \mathbf{c})$ is referred to as the circuit operator. (Note that for translation operations $\mathcal{W}^* = \mathcal{W}$.) The meaning of $\mathcal{C}$ is that, at the end of the sequence, the operator's coordinate frame has undergone the orthogonal operation $\mathbf{C}$ (rotation, reflection, inversion, identity) and his location is given by $\mathbf{f}$; *i.e.* $\mathcal{C}(\mathbf{I}, \mathbf{s}) = (\mathbf{C}, \mathbf{Cs} + \mathbf{c}) = (\mathbf{C}, \mathbf{f})$. Under the RH/FS convention (Frank, 1951) with the line direction ξ pointing outwards from the plane of the paper, line defects are characterized by $\mathcal{C}^{-1}$ (Pond & Hirth, 1994). For circuit 1 in Fig. 2(*a*), we obtain, using translation operations,

$$\begin{aligned}\mathcal{C}_1 &= (\mathbf{I}, 2\mathbf{a}_1)\\ &= (\mathbf{I}, \mathbf{a}_2)(\mathbf{I}, \mathbf{a}_2)(\mathbf{I}, -\mathbf{a}_3)(\mathbf{I}, -\mathbf{a}_3)\\ &\quad \times (\mathbf{I}, \mathbf{a}_1)(\mathbf{I}, \mathbf{a}_1)(\mathbf{I}, -\mathbf{a}_2)(\mathbf{I}, -\mathbf{a}_2)(\mathbf{I}, \mathbf{a}_3)(\mathbf{I}, \mathbf{a}_3).\end{aligned} \tag{1}$$

Hence, the defect encircled can be regarded as having dislocation content with Burgers vector $\mathbf{b} = -2\mathbf{a}_1$. Similarly, circuit 2 can be shown to correspond to $\mathcal{C}_2 = (\mathbf{I}, 4\mathbf{a}_1)$ and therefore it can be regarded as encircling dislocations with total $\mathbf{b} = -4\mathbf{a}_1$. Thus, the defect content of Fig. 2(*a*) can be modelled as a wall of edge dislocations with $\xi \| [0001]$, infinitesimal line length and each having $\mathbf{b} = -\mathbf{a}_1$. Alternatively, the circuits in Fig. 2 may be considered as comprising sequences of sixfold rotation operations $(\mathbf{6}^-, \mathbf{0})$ acting about *O*; thus, we have

$$\mathcal{C} = (\mathbf{6}^+, \mathbf{0}) = (\mathbf{6}^-, \mathbf{0})(\mathbf{6}^-, \mathbf{0})(\mathbf{6}^-, \mathbf{0})(\mathbf{6}^-, \mathbf{0})(\mathbf{6}^-, \mathbf{0}) \tag{2}$$

and $\mathcal{C}^{-1} = (\mathbf{6}^-, \mathbf{0})$, identifying the defect's 60° positive wedge disclination character. Note that, in this case, $\mathcal{C}$ is independent of the initial circuit dimensions, *i.e.* $\mathcal{C}_1 = \mathcal{C}_2 = (\mathbf{6}^+, \mathbf{0})$.

In the above discussion, the equivalence of disclinations and dislocation arrays has been demonstrated for graphene using circuit mapping. We now discuss ways to remove the disclination character through the introduction of admissible defects. Obviously, a series of dislocations having Burgers vector opposite to the one identified by (1) can be introduced for that purpose. Fig. 3(*a*) illustrates such an array, each dislocation having $\mathbf{b} = \mathbf{a}_1$. A second way is shown in Fig. 3(*b*) by an array of dislocations with Burgers vectors $1/3[1\bar{2}10]$ and $1/3[11\bar{2}0]$, the defects now comprising a tilt boundary. Their spacing h is consistent with the well known expression $\omega = 2\sin^{-1}(b/2h)$, where b is the magnitude of the Burgers vector and $\omega = 60°$ the strength of the disclination. The dislocation array introduced to remove the 60° positive wedge disclination is geometrically equivalent to a 60° negative wedge disclination (Eshelby, 1956; Li, 1972). The core of the 60° negative wedge disclination itself is realized in the form of a heptagon. Fig. 4(*a*) illustrates a pentagon–heptagon pair corresponding to a disclination dipole and circuit mapping can be employed to show that it does not have disclination character. In fact, the dipole corresponds to

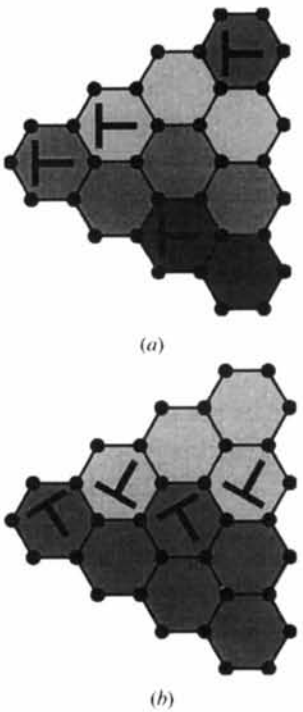

Fig. 3. (*a*) Array of edge dislocations, each having $\mathbf{b} = \mathbf{a}_1$, that can be introduced to remove the defect character from Fig. 2(*a*). (*b*) Equivalent array of dislocations having Burgers vectors $1/3[1\bar{2}10]$ and $1/3[11\bar{2}0]$; the dislocations comprise a tilt boundary.

a single dislocation with $\mathbf{b} = -\mathbf{a}_1$, as can be seen by mapping the closed circuit *s–t–u–v–w–x–s* (circuit 3) to the reference space (Fig. 4*b*). The circuit is expressed mathematically as

$$\begin{aligned} C_3 &= (\mathbf{I}, \mathbf{a}_1) \\ &= (\mathbf{I}, -2\mathbf{a}_1)(\mathbf{I}, 3\mathbf{a}_2)(\mathbf{I}, -3\mathbf{a}_3)(\mathbf{I}, 3\mathbf{a}_1) \\ &\quad \times (\mathbf{I}, -3\mathbf{a}_2)(\mathbf{I}, 3\mathbf{a}_3). \end{aligned} \tag{3}$$

If we increase the distance between pentagon and heptagon, more dislocations of $\mathbf{b} = -\mathbf{a}_1$ are inserted in a proportional manner.

We now move to discuss applications of the above to conformations exhibiting curvature. Pentagons and heptagons have been identified in these arrangements to introduce cap closure of tubes, changes in orientation of their axes, in their radius and in their helicity (Iijima, Ichihashi & Ando, 1992; Chico, Cresp, Benedict, Louie & Cohen, 1996). We treat these cases below.

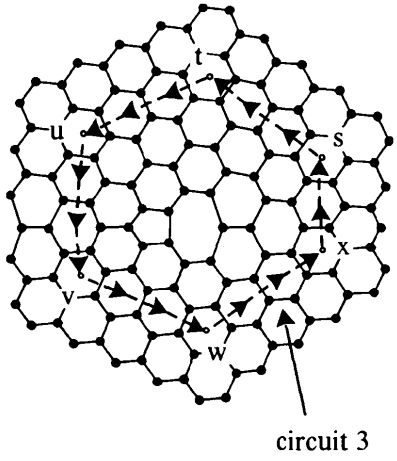

(*a*)

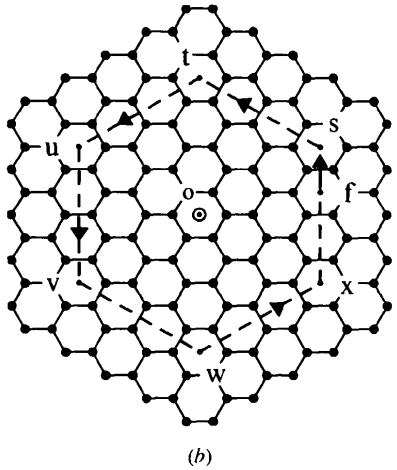

(*b*)

Fig. 4. (*a*) Closed circuit around a pentagon–heptagon pair. (*b*) The same circuit mapped in the reference space. The closure failure **fs** does not vary with distance from the core of the defect and hence signifies the defect's dislocation character ($\mathbf{b} = -\mathbf{a}_1$).

2.2. *Capping of single tubules*

Consider for example a simple single-sheet tubule capped by a portion of a C_{180} molecule terminated with the zig-zag structure (Saito, Fujita, Dresselahaus & Dresselahaus, 1992) as shown in Fig. 5(*a*). As known, six pentagons are required for cap closure in accordance with Euler's constraints. Hence, the cap is a disclination multipole. We can identify its overall defect character by circuit mapping. A closed circuit is illustrated in Fig. 5(*a*) around one of the six disclinations. In addition, a closed circuit starting at *A* and running around the circumference of the tubule is shown. In circuit mapping, the choice of reference space is crucial. Here we can map our circuits into an infinite graphene sheet or the uncapped tubule. Each mapping gives its own information as explained below.

Fig. 5(*b*) shows the circuits mapped in graphene. A pole disclination can always be identified (irrespective of cap shape) and its core is taken as origin. The positions of the other five disclinations with respect to this origin are indicated and the material removed for the creation of each disclination is shaded. One closed circuit is constructed around each disclination and the respective closure failures $\mathbf{f}_i\mathbf{s}_i$ ($i = 0, \ldots, 5$) are indicated. These increase with distance from the pole of each corresponding individual disclination as explained in §2.1. The defect character of the disclination multipole can be identified by considering the closed circuit around the whole configuration, *i.e.* the circumferential circuit. This circuit maps in the reference space as five disjoint segments $\mathbf{A}_j\mathbf{A}_{j+1}$, which are interrelated by 60° rotations about the origin. The segments can be connected by adding the disclination closure failures $\mathbf{f}_i\mathbf{s}_i$. We observe that the total closure failure is then always given by the vector **FS** indicated in Fig. 5(*b*) for any distance from the origin. In other words, the disclination multipole exhibits dislocation character but not disclination character (although the individual disclinations exist), since disclinations have ever increasing closure failure with increasing distance from the origin. The multipole's dislocation character depends on the distance of the five disclinations from the one at the pole and this is similar to the pentagon–heptagon case. In other words, the total Burgers vector increases with increasing distance of the disclinations. Hence, the defect character of an isolated 60° positive wedge disclination can be annihilated by the addition of either one negative wedge disclination or a multipole of five positive wedge disclinations. The cap shape is determined by its overall defect content and the distribution of the component defects; the latter are in turn determined by the tubule radius and helicity.

An alternative reference space for mapping is the uncapped tubule. Such mapping can give us information

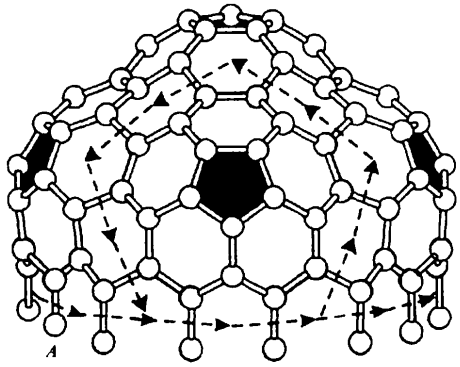

(a)

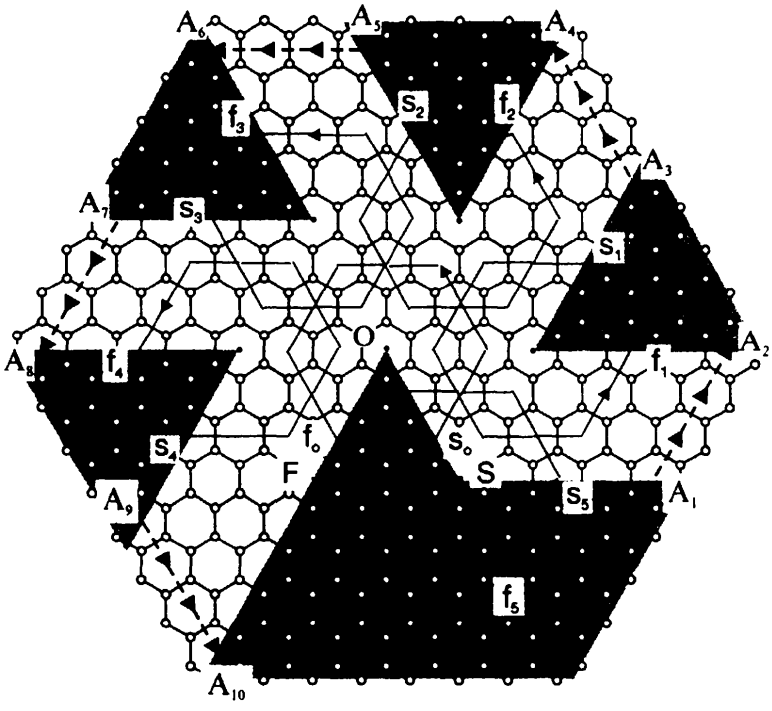

(b)

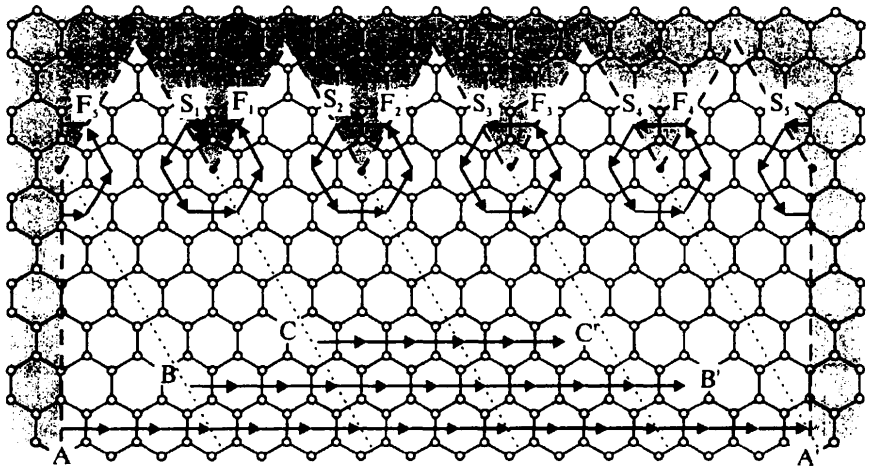

(c)

Fig. 5. (*a*) Single-sheet tubule having the zig-zag structure and capped by half a C_{180} molecule. Closed circuits are indicated around one of the six pentagons and around the circumference of the tubule. (*b*) Circuits around the cap disclinations mapped in graphene. The origin is taken to be at the pole disclination. The positions of the rest disclinations are indicated by black circles. The material removed for the creation of each disclination is shaded. Disclination closure failures are denoted as $\mathbf{f}_i\mathbf{s}_i$ ($i = 0, \ldots, 5$). Segments $\mathbf{A}_j\mathbf{A}_{j+1}$ ($j = 1, \ldots, 9$) correspond to mapping of the circumferential circuit of the tubule. The total closure failure for this circuit is always **FS**. (*c*) Mapping in the uncapped tubule. A circumferential circuit maps as open segment $\mathbf{AA}'$. The positions of the five circumferential disclinations are indicated by black circles. The defect content required to fit the cap on the tubule is given by the reduction in segment length from $\mathbf{AA}'$ to $\mathbf{BB}'$ to $\mathbf{CC}'$. Dotted lines delineate the white sectors shown in (*b*).

on the material that must be removed from the uncapped tubule to introduce capping. Fig. 5(*c*) shows the tubule opened out flat and we map our circuits there for convenience. A closed circuit around the tubule circumference maps as open segment $\mathbf{AA}'$ in this reference. The positions of the five circumferential disclinations are then arranged along a line and the pole disclination degenerates into five distinct points. The combination of the disclination closure failures gives the reduction in length of $\mathbf{AA}'$, *i.e.* the dislocation content required to fit the cap on the tubule. Thus, $\mathbf{AA}'$ reduces to $\mathbf{BB}'$ and then to $\mathbf{CC}'$ while moving towards the top of the cap. We emphasize that this defect content is defined with respect to circumferential vector $\mathbf{AA}'$. We can regard the cap to be fitted on the tubule *via* a one-dimensional graded epitaxic interface with the defects being introduced in order to accommodate the removal of material. Then, the Frank–Bilby method of circuit mapping (Christian, 1981; Pond & Hirth, 1994) can be applied for the characterization of its defect content, whereby $\mathbf{AA}'$ is the probe vector along the interface. The reduction in length of $\mathbf{AA}'$ gives the total defect content intersected by the probe vector.

The defect character of any cap can be established in the way presented above.

2.3. *Defects introducing changes in tubule helicity, radius and orientation*

Here we demonstrate the possibility of predicting changes in tubule parameters as a function of its defect content using circuit mapping. The convention adopted for helicity in the literature recently in terms of the helix angle α or hexagon indexing (Saito, Fujita, Dresselahaus & Dresselahaus, 1992) is very closely related to circuit mapping. According to such indexing, any tubule is described by a pair of integers (m, n) defining the location of the lattice point to be superimposed on the origin when rolling a graphene sheet to form the tubule. In order to keep a one-to-one correspondence, we confine the argument to angles $\alpha \leq 30°$, according to graphene symmetry. When the tubule axis is parallel to a mirror line of the sheet, then $\alpha = 0°$, *i.e.* zero helicity.

Circumferential circuits such as the one shown in Fig. 5(*a*) map to become lines such as $\mathbf{AA}'$ in Fig. 6(*a*) when the tubule is unwrapped. However, if the tubule axis is inclined to a mirror line, such circuits map to forms like $\mathbf{AA}''$. Let the helicity angle be defined as the angle $\alpha = \angle(\mathbf{a}_1, \mathbf{AA}')$. In general, any circumferential vector can always be written as $\mathbf{AA}' = m\mathbf{a}_1 + n\mathbf{a}_2$, where $\mathbf{a}_1 = 1/3[2\bar{1}\bar{1}0]$ and $\mathbf{a}_2 = 1/3[\bar{1}2\bar{1}0]$ (note that $\mathbf{a}_3$ is linearly dependent on $\mathbf{a}_1$ and $\mathbf{a}_2$). For $0 \leq \alpha \leq 30°$, we need to consider only $m/2 \geq n \geq 0$. The tubule radius is given by $R_{mn} = |\mathbf{AA}'|/2\pi = (a_h/2\pi)(m^2 + n^2 - mn)^{1/2}$, where $a_h = 2.455$ Å, the lattice parameter of graphene (see Appendix *A*). The tubule axis is defined by the vector $\mathbf{N}_{mn}$ perpendicular to $\mathbf{AA}'$, *i.e.*, in Miller–Bravais indices, $\mathbf{N}_{mn} = [n, \bar{m}, (m-n), 0]$. The helicity angle is given by (see Appendix *A*)

$$\alpha = \cos^{-1}\left[(2m - n)/2(m^2 + n^2 - mn)^{1/2}\right] = \cos^{-1}\left[a_h(2m - n)/4\pi R_{mn}\right]. \quad (4)$$

We consider changes in α, R_{mn} and $\mathbf{N}_{mn}$, introduced by dislocation arrays composed of dislocations having primitive Burgers vectors, *i.e.* equal to $\mathbf{a}_1$ and/or $\mathbf{a}_2$. We remind the reader that such arrays correspond to combinations of pentagon–heptagon pairs as shown above. The distance between pentagon and heptagon and their axial orientation defines the total Burgers vector of the pair.

Let the total defect content introducing the change be characterized by Burgers vector $\mathbf{b} = b_1\mathbf{a}_1 + b_2\mathbf{a}_2$, where b_1 and b_2 are integers. If the tubule prior to the introduction of the defects is described by the integers (m, n), we assume that the final tubule is described by integers (f, g); the latter pair defines any changes to helicity, radius and tubule axis from the expressions given above. The junction between the two tubules is taken up by pentagons and heptagons of total Burgers vector $\mathbf{b}$. We regard this region as a one-dimensional interface as illustrated in Fig. 6(*b*), which shows the two tubules opened out flat. It can be shown that (f, g) is related to (m, n) and (b_1, b_2) as well as to the relative angle φ of the axes of the initial and final tubule. For our purpose, the Frank–Bilby method for circuit mapping is applied in the manner described by Pond & Hirth (1994), as explained analytically below.

We designate the initial tubule black (μ) and the final one white (λ). We then consider for simplicity the interface line to coincide with the circumferential vector of tubule μ and we define the defect content $\mathbf{b}$ for this particular choice. A closed circuit *S–L–M–N–O–S* encircling the interface (and hence the defects) is shown in Fig. 6(*b*). The sense of the circuit is taken to agree with the RH/FS convention for bicrystals (Pond & Hirth, 1994) with the line direction ξ of the defects pointing outwards from the plane of the paper. This same convention also defines the senses of the circumferential vectors **NS** and **PN** of μ and λ, respectively. The circuit is shown mapped in the reference space in Fig. 6(*c*). A closure failure **FS** arises after mapping, corresponding to the total defect content $\mathbf{b}$ encircled.

The closure failure is identified mathematically as follows: the white circuit segment reduces to the vector $\mathbf{SN} = \mathbf{v}^r$ (the superscript signifies that the vector is expressed in the coordinate frame of the reference space). Similarly, the black circuit segment reduces to $\mathbf{NS} = -\mathbf{v}^r$. When mapped from their respective lattices to the reference, these vectors are $\mathbf{P}_\lambda^{-1}\mathbf{v}^r$ and $-\mathbf{P}_\mu^{-1}\mathbf{v}^r$, respectively, where $\mathbf{P}_\lambda$ and $-\mathbf{P}_\mu$ are the transformations by which the white and black lattices are obtained from the reference. Hence, the circuit operator reduces in this case to $\mathcal{C} = (\mathbf{I}, \mathbf{P}_\lambda^{-1}\mathbf{v}^r - \mathbf{P}_\mu^{-1}\mathbf{v}^r) = (\mathbf{I}, \mathbf{SN} + \mathbf{NF})$. The

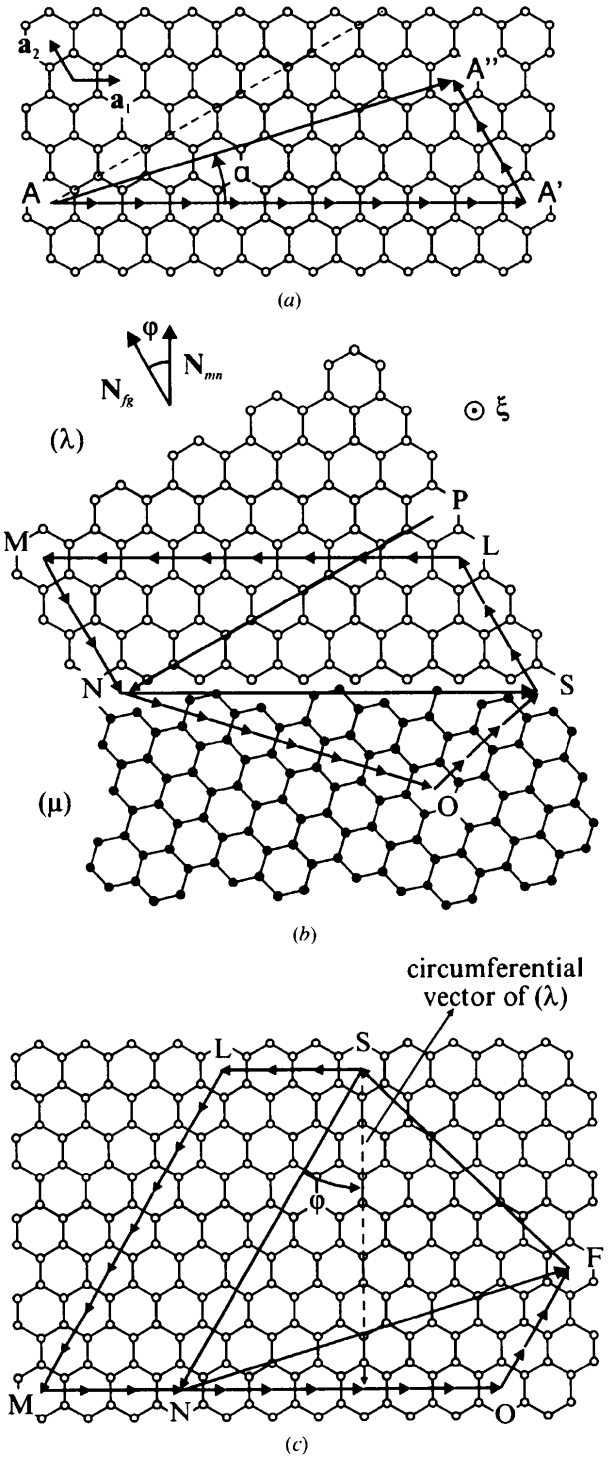

Fig. 6. (*a*) Mapping of circumferential circuits of tubules with and without helicity (**AA**$''$ and **AA**$'$, respectively). The dashed line denotes the maximum helicity angle $\alpha = 30°$. (*b*) Unreconstructed interface between two tubules, λ and μ, of different radius, orientation and helicity, shown after the tubules have been opened out flat. **PN** and **NS** are the circumferential vectors of tubules λ and μ, respectively. (*c*) Mapping of the closed circuit of (*b*) in the reference space. Closure failure **FS** arises.

defect content is identified by $\mathcal{C}^{-1}$ and therefore

$$\mathbf{b}^r = \mathbf{P}_\mu^{-1}\mathbf{v}^r - \mathbf{P}_\lambda^{-1}\mathbf{v}^r. \tag{5}$$

The vector $\mathbf{v}^r$ is known as the probe vector. Mapped vectors have in the reference space the same indices as in their respective lattices as explained in detail elsewhere (Pond & Hirth, 1994). Through transformations $\mathbf{P}_\lambda$ and $\mathbf{P}_\mu$, the relative rotation and deformation of the two lattices is taken into account. However, a multiplicity of equivalent descriptions is possible, all being consistent with the same physical interface (although descriptions for which the component defects are relatively widely spaced should be more useful). For example, note that in the mapping of Fig. 6(*c*) our choice of the relative rotation angle is not the smallest possible; this has been done deliberately in order not to overcrowd a small area of the diagram. The choice of reference lattice is itself arbitrary, but (5) can be further simplified if either the white or the black lattice is chosen as reference, in which case one of $\mathbf{P}_\lambda$ and $\mathbf{P}_\mu$ is equal to **I**.

We proceed by substituting in (5) $\mathbf{b}^r = b_1\mathbf{a}_1 + b_2\mathbf{a}_2$ and $\mathbf{P}_\mu^{-1}\mathbf{v}^r = m\mathbf{a}_1 + n\mathbf{a}_2$. Hence, we obtain $\mathbf{P}_\lambda^{-1}\mathbf{v}^r = (m - b_1)\mathbf{a}_1 + (n - b_2)\mathbf{a}_2$. The circumferential vector of the white tubule forms an angle φ with $\mathbf{SN} = \mathbf{P}_\lambda^{-1}\mathbf{v}^r$. Then, from the scalar product of **SN** and **PN**, we obtain

$$\begin{aligned}\varphi = \tan^{-1}\{3^{1/2}[(n - b_2)f - (m - b_1)g] \\ \times [(2m - 2b_1 - n + b_2)f \\ + (2n - 2b_2 - m + b_1)g]^{-1}\}.\end{aligned} \tag{6}$$

Hence, changes in helicity, orientation, and radius of the tubule depend, for a given initial pair (m, n), on the total defect content. The final expression is a completely general one and does not depend on the particular location of the interface line that was chosen initially. Equation (6) also takes into account the epitaxic fit of tubules having different radii. The applicability of (6) is illustrated in a simple example whereby we consider changes in radius and helicity while keeping $\varphi = 0°$. Hence, we obtain $f/g = (m - b_1)/(n - b_2)$ from which all permissible combinations can be obtained.

3. Defects in three-dimensional structures

§2 dealt with the defect character of isolated carbon tubules. The constraints imposed by their defect content must be adhered to when we move on to multilayered tubes. In order to investigate the complementarity between defect models in two- and three-dimensional structures, we now assume that the interactions between adjacent layers in multisheet structures are sufficient to lead to localized defect cores and explore the defect content of the experimentally observed configurations. We consider initially the model of concentric seamless tubules and capping of such buckytubes. We then dis-

cuss the scroll model. The papier-mâché model can be considered as composed of areas approximating either the seamless or the scroll model and so it is not treated separately.

3.1. *Concentric seamless tubules and multisheet caps*

Consider first seamless tubules with a common axis; we assume that the sheets are separated by $c_h/2$, where c_h is the lattice constant of hexagonal graphite normal to the basal plane, and that their interaction leads to the characteristic ... *ABAB*... stacking sequence of graphite. Following Zhang *et al.* (1993), the circumference of the $(n + 1)$th tubule is πc_h larger than the nth one ideally and this is independent of n. Thus, the magnitude of the additional Burgers vector per layer is πc_h and is directed tangentially to the layer (*i.e.* in the orientation perpendicular to the tube axis and locally parallel to the basal plane according to the observer). Hence, the length difference between adjacent sheets is accommodated by edge dislocations and, in order to minimize elastic energy, these are likely to have minimum magnitude of **b**. Fig. 7(*a*) illustrates a buckytube having a $\langle 1\bar{1}00\rangle$ axis, *i.e.* a zigzag arrangement of atoms along the circumference. For this case, the edge dislocations have $\mathbf{b} = 1/3\langle\bar{1}\,\bar{1}20\rangle$. It can be seen that the 'extra half-planes' adopt a 'cooling-fin' configuration. In this particular figure, it is assumed that the edge dislocations lying in adjacent sheets are arranged in eight 45° tilt boundaries, separating regions of ... *ABAB*... graphitic alignment. Such arrangements are likely to be favourable due to elastic interactions. The number of tilt boundaries depends on the spacing and distribution of the component defects in accordance with the expression $\theta = 2\sin^{-1}(b/2h)$, where θ is the tilt angle, b is the magnitude of **b** and h is the spacing of the dislocations. The tilt-boundary assumption is justified by experimental observations of terminating fringes tending to align along radial lines in tubes that appear to polygonize (Bursill, Stadelmann, Peng & Prawer, 1994). It is interesting to note that the tilt angle associated with the total array (*i.e.* amounting to a single tilt boundary) is given by $\theta = 2\sin^{-1}\{\pi c_h/[2(c_h/2)]\} = 360°$, where $b = \pi c_h$ is the magnitude of additional Burgers vector **b** per layer and $h = c_h/2$. Thus, the dislocations in these arrays can be regarded as comprising a single 360° tilt boundary. A closed circuit is indicated in Fig. 7(*a*) around one of the 45° tilt boundaries. The circuit is shown mapped in the reference space (hexagonal graphite) in Fig. 7(*b*), whereby the defect content encircled is given by **FS**. Such mapping is consistent with the Frank–Bilby method for the defect content of interfaces (Christian, 1981; Pond & Hirth, 1994). Fig. 7(*c*) illustrates the whole tube mapped on the reference space, *i.e.* in hexagonal graphite, and the 'extra half-planes' comprising the 360° tilt wall are shown concentrated in one single array (shaded). We also note that this array cannot be modelled in terms of disclinations since there are no rotation operations in the reference space with appropriate orientation (*i.e.* along the tube axis).

The dislocations considered above are edge ones. However, for the ... *ABAB*... stacking, screw components of the Burgers vector can also exist. In this event, the helix angle α changes locally by $\tan^{-1}(b_s/2\pi R)$, where R is the tubule radius and b_s the magnitude of the screw component of the Burgers vector.

As pointed out by Zhang *et al.* (1993), the number of defects for each layer must be integral. However, in the case of a $\langle 1\bar{1}00\rangle$ tube considered above, the total defect content required for the accommodation of each layer is not integral since $\pi c_h/a_h \cong 8.6$. The remaining length difference between adjacent sheets has to be accommodated by straining the layers in a manner similar to epitaxic fit. The strain can be relieved by the introduction of one extra dislocation every two layers. If the tube axis were $\langle\bar{1}\,\bar{1}20\rangle$, the number of defects required for complete accommodation would be integral (since $\pi c_h/3^{1/2}a_h \cong 5$) and would be composed of $1/3\langle\bar{2}110\rangle/1/3\langle\bar{1}2\bar{1}0\rangle$ perfect dislocation pairs. Note that these defects have screw components of opposite sign that would cancel if paired but otherwise would modify the local value of α. For concentric tubes where the axis is not parallel to $\langle\bar{1}\,\bar{1}20\rangle$ or $\langle 1\bar{1}00\rangle$, the 'cooling-fin' structure would persist but the dislocations would generally exhibit some screw character. Variations of the screw component from layer to layer would cause local modifications to the helix angle α.

The defects considered here are dislocations admissible in the ordinary graphite structure (although $1/3\langle\bar{1}\,\bar{1}20\rangle$ dislocations can decompose into pairs of partials with Burgers vectors $1/3\langle\bar{1}010\rangle$ and $1/3\langle 0\bar{1}10\rangle$, separated by stacking faults). None of the perfect or partial dislocations considered require the breaking of C—C bonds. An alternative defect model has also been proposed utilizing a 'wide interfacial dislocation' concept (Zhang *et al.*, 1993).

We now move to discuss the defect structure of multisheet caps for multilayered tubes composed of seamless tubules. Two issues arise; first, there is the defect content required to form a hemispherical (or equivalent) structure, as described earlier for a single sheet and, second, the content needed to accommodate successive layers as described above for concentric tubules. With respect to the latter, the 'cooling-fin' structure of edge dislocations having basal-plane Burgers vectors can be extended to accommodate the conformation of sequential caps. A second orthogonal set of edge dislocation loops would be necessary to accommodate the additional curvature in the cap. On the former, we remind the reader that the defect content introducing curvature to a single-sheet cap can be visualized in terms of disclinations or equivalent dislocation arrays. The line direction of those defects is normal to the sheet, although the line length for defects in such sheets

is vanishingly small. In extending this model to three-dimensional structures, it must be kept in mind that the admissible defects are now those characteristic of the graphite structure. However, 60° disclinations are not admissible defects in graphite, and hence the disclination model cannot be extended in this structure. Since a sixfold screw axis arises parallel to [0001] in graphite, only 60° dispirations (*i.e.* a 60° disclination combined with a screw partial dislocation with $\mathbf{b} = \mathbf{c}/2$) can arise. The same is true for the equivalent dislocation array, *i.e.* again a $\mathbf{b} = \mathbf{c}/2$ partial dislocation is required for restoration of the graphite structure. However, this would mean that the multisheet caps are no longer composed of seamless concentric layers; instead, layers are transformed into helical planes. Hence the structure of caps composed of seamless concentric layers is not hexagonal graphitic, *i.e.* even if the ... *ABAB*... stacking is preserved in the tube, it is destroyed in the cap.

3.2. *The scroll model*

We now examine the scroll model and the question to be answered is whether the hexagonal graphitic stacking can be preserved in a scroll. From the above discussion, we observe that a scroll can conveniently be capped by one 60° dispiration and five 60° disclinations. In fact, this is the only way to cap a scroll. Assuming that initially we have a cap composed of seamless concentric layers separated by $c_h/2$, the dispiration's translation part transforms it into a manifold of helical planes. Hence, the graphitic structure is preserved very locally at the cap, *i.e.* around the pole dispiration. However, the other five disclinations remain and so the graphitic structure is destroyed there. Moving to the tube itself, we remind the reader that the rotational character of all cap defects is cancelled as discussed in §2.2. Hence, only the $\mathbf{c}/2$ dislocation character remains. Although the dis-

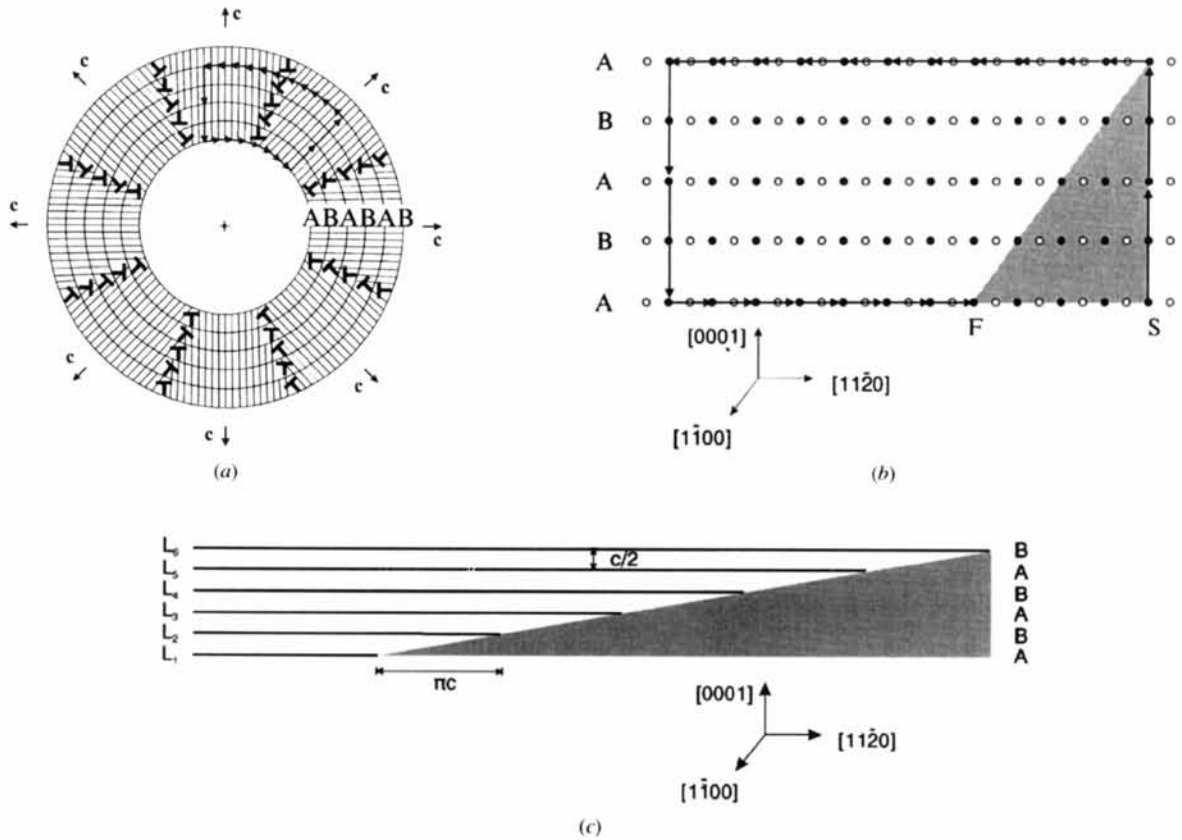

Fig. 7. (*a*) Schematic illustration of a buckytube having the zig-zag configuration (*i.e.* a $\langle 1\bar{1}00\rangle$ axis). The atomic positions correspond to line intersections. The graphitic ...*ABAB*... alignment is preserved locally through eight 45° tilt boundaries. Edge dislocations having $\mathbf{b} = 1/3\langle\bar{1}\bar{1}20\rangle$ are indicated. A closed circuit around one of the tilt boundaries is shown. (*b*) Mapping of the closed circuit in the reference space of single-crystalline hexagonal graphite ($\langle 1\bar{1}00\rangle$ projection; atoms at Miller–Bravais fractional coordinates 0, 0, 0, 1/4 and 1/3, −1/3, 0, 1/4 are unfilled and filled, respectively). The defect content of the boundary is given by **FS**. The material removed is shaded. (*c*) Mapping of the whole tube in the reference space. The defects (shaded) are now taken concentrated in one array corresponding to a 360° tilt wall. L_i denote layers and the stacking sequence is indicated.

placement $\mathbf{c}/2$ is rotated locally by 90° when going from the cap to the tube, the defect's line direction remains along the tube axis. So the dislocation is transformed into an edge-type Frank partial as discussed by Amelinckx, Bernaerts, Zhang, Van Tendeloo & Van Landuyt (1995). The defect array accommodating curvature is virtually identical to the one in the concentric seamless case, the 'extra half-planes' of the edge dislocations adopting a 'cooling-fin' configuration as in Fig. 7(*a*). If the number of defects in a given layer is less than sufficient to accommodate the circumferential strain, that particular sheet will experience a tensile stress. This may, in turn, affect the state of strain in other layers and could conceivably cause scrolls to wind up. We note that the edge dislocations described above are 'glissile' in the basal planes.

4. Conclusions

A multiplicity of defects has been described for buckytubes and carbon nanoparticles. If combined, they could lead to complex configurations such as the papier-mâché structures. Even in cases where the defect population is large, dislocation theory can provide simpler descriptions for modelling purposes than a disordered graphite description. We now discuss the relevance of our results for the interpretation of experimental observations.

It is generally accepted that buckytubes thicken through the epitaxic addition of layers. Initially formed islands grow to full layers by the preferential addition of C atoms at surface ledges. Such layers may develop into seamless tubules or scrolls (Amelinckx, Bernaerts, Zhang, Van Tendeloo & Van Landuyt, 1995). A commonly observed feature of multilayered nanotubes is the occurrence of multiple helicities within the same tube (*e.g.* Bursill, Stadelmann, Peng & Prawer, 1994). This is consistent with a graphitic alignment and can be introduced by appropriate defects. An alternative explanation has been proposed by Zhang *et al.* (1993), whereby a two-dimensional coincidence-site interface between adjacent graphene sheets is assumed. The suitable coincidence position can be found by relative rotation and translation of the sheets. Calculations show that such relative motion may be easy at room temperature (Charlier & Michenaud, 1993); on the other hand, it may be inhibited by factors such as polyhedral cap shape and re-entrant parts at the contact between the buckytube and its substrate (Amelinckx, Bernaerts, Zhang, Van Tendeloo & Van Landuyt, 1995). Hence, both models may be appropriate depending on various factors such as growth conditions, capping, curvature *etc.*

In conclusion, the defect character of carbon nanotubes and nanoparticles has been studied under the topological framework of line defects in crystals and interfaces and the complementarity between two-dimensional and three-dimensional models has been investigated. For isolated seamless tubules, it has been shown that changes in radius, orientation and helicity depend on the defects introduced and, in particular, 60° disclinations and dislocations with basal-plane Burgers vectors, having line direction along the tube local normal [0001]. In multilayered tubes, the hexagonal graphite stacking sequence can be preserved through the introduction of dislocations having tangential basal-plane Burgers vectors that introduce curvature accommodation in adjacent sheets. Such defects have line direction along the tube axis. They can also possess additional screw character that changes the helicity locally between layers. Elastic interactions probably favour their arrangement in tilt boundaries. These boundaries can lead to polygonization for large radii. In multilayered caps, the graphite structure is not conserved since the defects required for cap closure are 60° disclinations and these are not admissible in graphite. The scroll structure has the same overall defect content as the seamless tube and can be considered to be obtained through the introduction of a Frank partial in an originally seamless tube. The Frank partial is the consequence of the existence of a (60°, $\mathbf{c}/2$) dispiration in the cap, which is an admissible graphite defect.

The multiplicity of defects possible can lead to complex configurations, in agreement with published experimental observations. While there are no detailed analyses of linear defects in nanotubes, several groups have reported various observations of such defects (*e.g.* Dravid *et al.*, 1993; Zhou *et al.*, 1994; Amelinckx, Bernaerts, Zhang, Van Tendeloo & Van Landuyt, 1995). We expect more will follow with the rigour necessary for crystallographic analysis. Further experimental observations are particularly necessary for the case of multilayered nanotubes and nanoparticles. For the case of single-layered tubules, it remains to link arrays of pentagons and heptagons with changes in tubule geometric parameters. All this information could provide insight into growth mechanisms. The effect of defects and the possibility of graphitic stacking on the electrical properties of these materials also remains to be investigated.

This work has been supported under EU contract ERBCHRX-CT94-0467. One of the authors (RCP) is grateful to Northwestern University for support through an Eshbach scholarship. A second author (VPD) is supported by NSF-NYI program, grant no. DMR-9357513.

APPENDIX *A*

The circumferential vector can be written as

$$\mathbf{AA}' = (1/3)[(2m - n), (2n - m), -(m + n), 0]. \quad (7)$$

The tubule radius is then given by $R_{mn} = |\mathbf{AA}'|/2\pi$ and, using Frank's 4-space method for calculations in

hexagonal materials (Pond, Aindow & Clark, 1987), we obtain

$$R_{mn} = (|\mathbf{e}|/6\pi)[(2m - n)^2 + (2n - m)^2 + (m + n)^2]^{1/2}, \quad (8)$$

where $|\mathbf{e}| = (3/2)^{1/2}a_h$. Hence,

$$R_{mn} = (a_h/2\pi)[m^2 + n^2 - mn]^{1/2}. \quad (9)$$

If we define helicity as $\alpha = \angle(\mathbf{a}_1, \mathbf{AA}'')$ then, from the scalar product (Pond, Aindow & Clark, 1987), we obtain

$$\alpha = \cos^{-1}\Big(\big[-2(n - 2m) + (m - 2n) + (m + n)\big] \times \{6^{1/2}[(n - 2m)^2 + (m - 2n)^2 + (n + m)^2]^{1/2}\}^{-1}\Big), \quad (10)$$

from which (4) is obtained.

References

Amelinckx, S., Bernaerts, D., Zhang, X. B., Van Tendeloo, G. & Van Landuyt, J. (1995). *Science*, **267**, 1334–1338.

Blase, X., Benedict, L. X., Shirley, E. L. & Louie, S. G. (1994). *Phys. Rev. Lett.* **72**, 1878–1881.

Bursill, L. A., Peng, J. L. & Fan, X. D. (1995). *Philos. Mag.* A**71**, 1161–1176.

Bursill, L. A., Stadelmann, P. A., Peng, J. L. & Prawer, S. (1994). *Phys. Rev. B*, **49**, 2882–2887.

Charlier, J. C. & Michenaud, J. P. (1993). *Phys. Rev. Lett.* **70**, 1858–1861.

Chico, L., Cresp, V. H., Benedict, L. X., Louie, S. G. & Cohen, M. L. (1996). *Phys. Rev. Lett.* **76**, 971–974.

Christian, J. W. (1981). *The Theory of Transformations in Metals and Alloys*. Pergamon Press.

Clinard, C., Rouzaud, J. N., Delpeux, S., Beguin, F. & Conard, J. (1994). *J. Phys. Chem. Solids*, **55**, 651–657.

Dravid, V. P., Lin, X., Wang, Y., Wang, X. K., Yee, A., Ketterson, J. B. & Chang, R. P. H. (1993). *Science*, **259**, 1601–1604.

Dresselahaus, M. S. (1992). *Nature (London)*, **358**, 195–196.

Ebbesen, T. W. (1994). *Annu. Rev. Mater. Sci.* **24**, 235–264.

Eshelby, J. D. (1956). *Solid State Phys.* **3**, 79–144.

Frank, F. C. (1951). *Philos. Mag.* **42**, 809–819.

Hahn, T. (1983). Editor. *International Tables for Crystallography*, Vol. A. Dordrecht: Kluwer Academic Publishers.

Hamada, N., Sawada, S. & Oshiyama, A. (1992). *Phys. Rev. Lett.* **68**, 1579–1581.

Harris, P. J. F., Green, M. L. H. & Tsang, S. C. (1993). *J. Chem. Soc. Faraday Trans.* **89**, 1189–1192.

Iijima, S. (1991). *Nature (London)*, **354**, 56–58.

Iijima, S., Ichihashi, T. & Ando, Y. (1992). *Nature (London)*, **356**, 776–778.

Kroto, H. W., Heath, J. R., O'Brien, S. C., Curl, R. F. & Smalley, R. E. (1985). *Nature (London)*, **318**, 162–163.

Li, J. C. M. (1972). *Surf. Sci.* **31**, 12–26.

Liu, M. & Cowley, J. M. (1994). *Ultramicroscopy*, **53**, 333–342.

Lu, J. P. (1995). *Phys. Rev. Lett.* **74**, 1123–1126.

Olk, C. H. & Heremans, J. P. (1994). *J. Mater. Res.* **9**, 259–262.

Pond, R. C., Aindow, M. & Clark, W. A. T. (1987). *Scr. Metall.* **21**, 971–974.

Pond, R. C. & Hirth, J. P. (1994). *Solid State Phys.* **47**, 287–365.

Reznik, D., Olk, C. H., Neumann, D. A. & Copley, J. R. D. (1995). *Phys. Rev. B*, **52**, 116–124.

Ruoff, R. S. (1994). *Nature (London)*, **372**, 731–732.

Saito, R., Fujita, M., Dresselahaus, G. & Dresselahaus, M. S. (1992). *Appl. Phys. Lett.* **60**, 2204–2206.

Tsang, S. C., Harris, P. J. F. & Green, M. L. H. (1993). *Nature (London)*, **362**, 520–522.

Ugarte, D. (1992). *Nature (London)*, **359**, 707–709.

Xie, S., Li, N., Zhang, Z., Liu, W., Wang, G., Qian, S. & Fu, C. (1995). *J. Mater. Sci.* **30**, 2291–2295.

Zhang, X. F., Zhang, X. B., Van Tendeloo, G., Amelincx, S., Op de Beeck, M. & Van Landuyt, J. (1993). *J. Cryst. Growth*, **130**, 368–382.

Zhou, O., Fleming, R. M., Murphy, D. W., Chen, C. H., Haddon, R. C., Ramirez, A. P. & Glarum, S. H. (1994). *Science*, **263**, 1744–1747.